J. Micromech. Microeng. **23** (2013) 065001 (14pp) doi:10.1088/0960-1317/23/6/065001

A recoil resilient lumen support, design, fabrication and mechanical evaluation

Arash Mehdizadeh[1,4], **Mohamed Sultan Mohamed Ali**[2,3], **Kenichi Takahata**[2], **Said Al-Sarawi**[1,4] **and Derek Abbott**[1]

[1] School of Electrical and Electronic Engineering, The University of Adelaide, SA 5005, Australia
[2] Department of Electrical and Computer Engineering, University of British Columbia, BC V6T 1Z4, Canada
[3] Faculty of Electrical Engineering, Universiti Teknologi Malaysia, 81310 Skudai, Johor, Malaysia

E-mail: arash@eleceng.adelaide.edu.au, sultan_ali@fke.utm.my, takahata@ece.ubc.ca, alsarawi@eleceng.adelaide.edu.au and dabbott@eleceng.adelaide.edu.au

Received 31 December 2012, in final form 10 March 2013
Published 22 April 2013
Online at stacks.iop.org/JMM/23/065001

Abstract
Stents are artificial implants that provide scaffolding to a cavity inside the body. This paper presents a new luminal device for reducing the mechanical failure of stents due to recoil, which is one of the most important issues in stenting. This device, which we call a recoil-resilient ring (RRR), is utilized standalone or potentially integrated with existing stents to address the problem of recoil. The proposed structure aims to minimize the need for high-pressure overexpansion that can induce intra-luminal trauma and excess growth of vascular tissue causing later restenosis. The RRR is an overlapped open ring with asymmetrical sawtooth structures that are intermeshed. These teeth can slide on top of each other, while the ring is radially expanded, but interlock step-by-step so as to keep the final expanded state against compressional forces that normally cause recoil. The RRRs thus deliver balloon expandability and, when integrated with a stent, bring both radial rigidity and longitudinal flexibility to the stent. The design of the RRR is investigated through finite element analysis (FEA), and then the devices are fabricated using micro-electro-discharge machining of 200-μm-thick Nitinol sheet. The standalone RRR is balloon expandable *in vitro* by 5–7 Atm in pressure, which is well within the recommended *in vivo* pressure ranges for stenting procedures. FEA compression tests indicate 13 $\times$ less reduction of the cross-sectional area of the RRR compared with a typical stainless steel stent. These results also show perfect elastic recovery of the RRR after removal of the pressure compared to the remaining plastic deformations of the stainless steel stent. On the other hand, experimental loading tests show that the fabricated RRRs have 2.8 $\times$ radial stiffness compared to a two-column section of a commercial stent while exhibiting comparable elastic recovery. Furthermore, testing of *in vitro* expansion in a mock artery tube shows around 2.9% recoil, approximately 5–11 $\times$ smaller than the recoil reported for commercial stents. These experimental results demonstrate the effectiveness of the device design for the targeted luminal support and stenting applications.

(Some figures may appear in colour only in the online journal)

1. Introduction

After the introduction of interventional cardiology in 1977, this discipline has been primarily driven forward by advances in stents since 1990 [1]. Stents are mechanical implants that provide chronic support against the lumen walls of their deployment site [2]. Further to their major use in the coronary artery disease [2], they are also widely used in ducts and lumens from other parts of the body [3–5].

There are over 100 different stent designs in the market today, though they can be categorized into general groups by their intended deployment area and manufacturing process. The general manufacturing process can be classified based

[4] Authors to whom any correspondence should be addressed.

on the (i) materials used, (ii) the primary form in which the materials come such as tubes, sheets or wires, (iii) the fabrication method including but not limited to laser machining, wire knitting and braiding or micro-electrical discharge machining (μEDM), (iv) geometry of the structures including majorly coils and slotted-tubes, and (v) some additional coating steps to address radiopacity and drug delivery [6].

Balloon-expandable (BE) stents are made out of plastically deformable materials. After expansion the stent retains its shape, though will lose some of its cross-sectional area (CSA) through recoil due to the elastic portion of the deformation [6, 7]. Elastic recoil is defined as the change in the mean CSA of a stent just before deflation of the angioplasty balloon at its highest pressure and after deflation and retraction of the balloon [8]. The ideal material and structures for BE stents should have a low yield stress to allow the stent to transform into its required shape, as well as high elastic modulus for minimal recoil [6, 9]. Clearly these two requirements are somewhat contradictory resulting in a challenge in stent design.

Despite the widespread use of high-pressure coronary stents in today's vascular interventions, these implants usually fail to achieve 60% to 80% of their expanding balloon nominal CSA [7]. In ideal situations with compliant lumens, with no signs of atherosclerosis, recoil has been reported to be the predominant mechanism causing failure of stents to achieve their nominal CSA [7]. The magnitude of recoil in stents is highly dependent on the design of the stent and ranges from 30% in coil stents to 16% in slotted-tube stents [7] increasing the risk of in-stent restenosis [10, 11]. As of today, restenosis also known as re-narrowing of the treated vessels is the most important post-intervention complication that limits the effectiveness of stenting; it has been reported to occur at rates up to 60% [10].

To improve stenting, several approaches have been adopted since the introduction of bare metal stents, including but not limited to drug eluting stents [12–16], self-expanding stents (SE) [17] and overexpansion techniques [7]; however, each tends to lead to different complications.

A meta-analysis concluded that drug eluting stents were associated with a greater mortality rate compared to that of bare metal stents due to late stent thrombosis [18]. BE stents are delivered in a crimped state and then morphed to a required dilated state. In order to compensate for the elastic recoil, cardiologists are usually required to overexpand the stent. This overexpansion may lead to complications such as early proliferation of endothelial cells around the distal points [19], as those points are the first to open in a typical angioplasty balloon expansion and thus apply more pressure to the arterial walls. Furthermore, it has been clinically shown that restenosis is in direct relation with the degree of injury inflicted upon the artery walls by the anatomic depth to which the stent strut penetrates the vessel wall thereby inducing trauma [11, 13]. Induced trauma and the resultant restenosis are also highly influenced by the stent design itself [20].

SE stents rely on the super-elasticity of materials such as austenite nickel–titanium alloys (Nitinol). These stents are mostly delivered in a constrained state to the deployment site, and then released for expansion [17]. They are fabricated to a diameter slightly larger than that of the target site and upon their delivery and expansion, they exert a low 'chronic' outward force against the vessel walls as the body temperature is beyond their transformation temperature (typically ~30 °C) [17, 21]. Although these stents could be custom-manufactured for a wide range of arteries, it is still difficult to tailor them to each individual patient's diseased artery specifications subject to different patterns of hardening and constriction. Furthermore, the use of these devices also can cause some level of overexpansion and injury to the treated arteries.

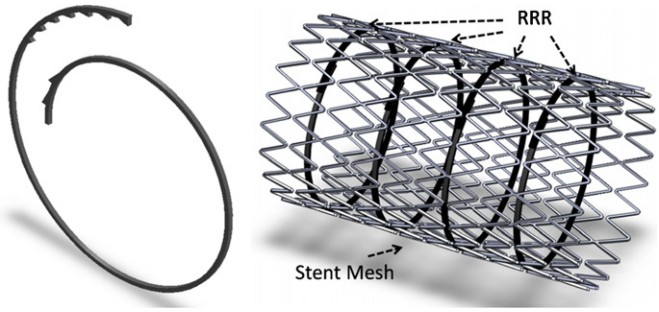

Figure 1. Recoil resilient ring (RRR) lumen support, (*a*) conceptual stand-alone model, (*b*) hosted by a commercial stent, RRRs are connected to the stent mesh by a single welding point. Stent mesh adopted from Open Stent Design [22].

Considering the limitations and requirements outlined above, there are gaps to cover in order to improve the recoil-related complications by targeting the design step of stent manufacturing. A new structure may be introduced to withstand large radial forces from both elastic recoil of the lumen and the stent itself while not sacrificing flexibility. Due to the availability of a vast number of state-of-the art designs, however, it is even more important to be able to harness the proven benefits of previously devised designs, while addressing their shortcomings with minimal introduction of new manufacturing or stent delivery techniques.

To address these, in this work we introduce recoil-resilient lumen supports we call recoil-resilient rings (RRR) as seen in figure 1(*a*). The RRRs are micro-fabricated from biocompatible alloy sheets to be used in their martensitic state[5] while inside the body. The design of the RRR is arranged to enable the integration of an array of the device with a vast range of today's state-of-the-art stents as an add-on to provide radial resilience. This design preserves longitudinal flexibility of stents while minimally affecting their production and deployment procedure.

In this study, the RRR devices are fabricated with Nitinol, a nickel-titanium shape-memory alloy (SMA) that has been adopted widely in today's medical implants and devices [23, 24] including SE stents [17, 21]. In this work, Nitinol is used in its martensitic state so that the device can be easily expanded by a balloon. Though widely used for SE stents, Nitinol alloy is also used in its martensitic

[5] Body and room temperatures lie well below the transformation temperature of Nitinol.

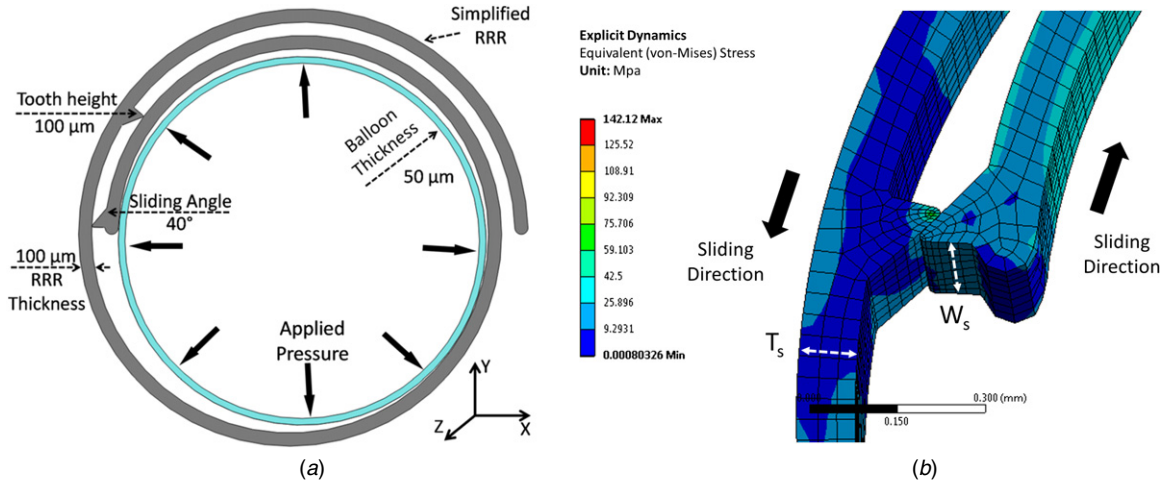

Figure 2. Finite element model of the simplified RRR, (*a*) flexible tube represents the angioplasty balloon, radial outward pressure is applied to the inner walls of the balloon during expansion, (*b*) dilation of the balloon causes the teeth to slide on each other at about 100 KPa in pressure facilitating expansion of the RRR.

form for construction of BE stents [6]. That is due to its high biocompatibility, corrosion resistance, radiopacity and comparable physical strength properties with regard to stainless steel, tantalum, platinum and cobalt alloys usually used in stent fabrication [6]. It is important to note that the choice of the material for this work is not because of its shape memory effect, but rather the *in vivo* benefits and flexibility in the martensitic state. Moreover, this brings potential for other possible expansion methods such as application of heat or electric current as well as remote actuation [25–27]. These possibilities are beyond the scope of this work.

Over the years, the demand toward production of non-traditional microstructures using μEDM has increased [28–30]. This method is used to produce microparts with sizes ranging from a few micrometers to several 100 μm. μEDM is a thermal process that can be used to cut electrically conductive materials utilizing intense heat provided by high-frequency pulses of miniaturized electrical discharge, enabling high precision and burr-free micromachining in any metal or alloy [28, 31]. The material biocompatibility of the machined pieces are not impaired by the μEDM thermal treatment [32]. Due to these benefits, μEDM has gained popularity in biocompatible micro-devices such as stents [6, 33, 34]. In this work, we exploited these features of μEDM to fabricate the proposed RRRs.

The rest of the paper is organized as follows. The design and modeling of RRR is discussed in section 2. The fabrication methodology, including shaping and heat treatment stages, are described in section 3. In section 4, the experimental results of the mechanical evaluation of the fabricated structure in comparison with a commercial stent are given, which is followed by the conclusion.

2. Design and modeling

The fabrication approach selected was μEDM of a Nitinol sheet, with 200 μm thickness, to produce a strip of the material that is to be shaped into the RRR. The RRR is an open overlapped ring. The two overlapping ends have a number of asymmetrical sawtooth structures facilitating sliding on top of each other in one direction when the RRR is opening. Upon contracting forces the teeth interlock so they keep the final expanded state. The design challenges are to develop a layout describable in a planar fashion that can be readily patterned using Nitinol sheets and a standard μEDM process, and then shape it according to the required description such that it resembles a ring for later crimping and deployment. It is also crucial to achieve various key mechanical characteristics including high radial stiffness for recoil resilience and low-pressure expandability that eliminates the need for high-pressure balloon expansion or over-expansions compensating for elastic recoil of BE stents.

Prior to any fabrication steps, we first study the effect of balloon expansion on a simplified model of the RRR device in a structural finite element analysis (FEA). Moreover, to investigate the effect of the proposed structures on the fluid regime, distribution of low wall shear stress as a predictor of later restenosis [35, 36] is studied in a computational fluid dynamic (CFD) analysis. These analyses provide a good framework for comparison of the performance of the proposed structure with a nominal current stent structure [22].

2.1. Structural analysis

2.1.1. Materials and methods. To simulate the expansion mechanics, the simplified design of the RRR with a short section of an elastic tube representing the angioplasty balloon, as shown in figure 2, is studied in a free expansion model [37] disregarding the lumen wherein the RRR is expanded as a stand-alone luminal support. The simulation is conducted by ANSYS finite element package (ANSYS Inc., Canonsburg, PA, USA) using a three-dimensional (3D) solid mechanics model with an explicit solver. To develop the model, the ring and balloon assembly were first developed in SolidWorks (SolidWorks Corp, Velizy, France) and then imported into ANSYS. In order to decrease the complexity of the model and for better convergence using the explicit solver, only two teeth

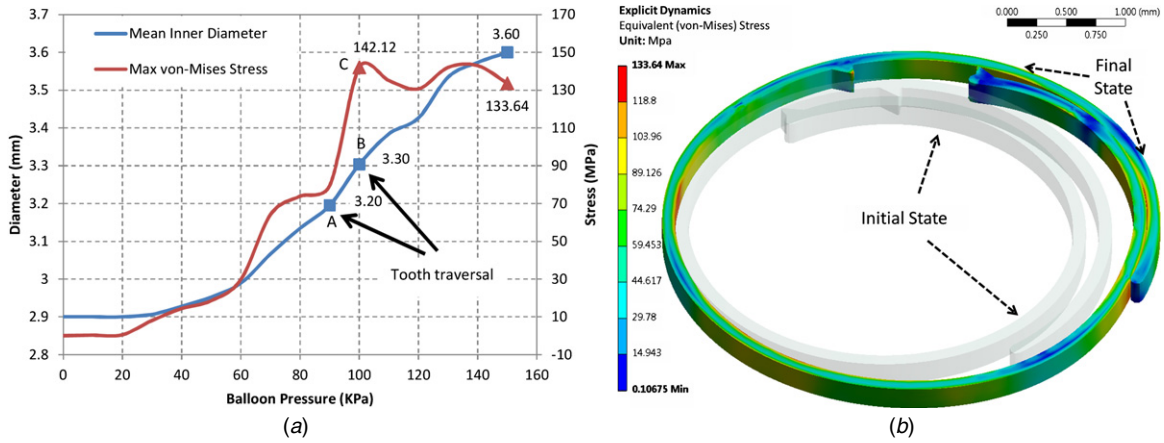

Figure 3. Radial displacement and stress results during expansion, (*a*) mean inner diameter of the RRR versus balloon pressure, and Max von-Mises stress versus pressure during the expansion period. Complete tooth traversal is observed at about 100 KPa pressure, (*b*) von-Mises stress contour plots of the expanded RRR at pressure 150 KPa.

Table 1. Material and geometrical properties of a typical BE stent model and RRR.

Material properties		
	RRR	**BE stent**
Material	Martensite Nitinol	Stainless Steel 316L
Density (gms cc^{-1})	6.5	8
Modulus of elasticity (GPa)	40	193
Poisson's ratio	0.3	0.3
Yield stress (MPa)	142	290
Tangent modulus (MPa)	714	2500
Tensile strength (MPa)	754	480
Geometrical properties		
Number of columns	1	2–10
Number of struts per columns	NA—regular ring	42 V-shaped
Strut width—W_s (μm)	200	80
Strut thickness—T_s (μm)	100	110

of the ring are modeled in this study. The detailed dimensional values of the model assembly are shown in figures 2(*a*) and (*b*). The width of the RRR in the *Z* direction is 200 μm (thickness of Nitinol sheet used for fabrication of RRR) whereas the balloon width is 0.5 mm with a thickness of 50 μm. The balloon is deployed inside the RRR so that it protrudes by 0.15 mm from the two sides of the RRR parallel to the *X*–*Y* plane.

For the simplified RRR, the material properties of Nitinol in the martensite state were chosen from the Nitinol sheet manufacturer (Memry Corp., Germany) in a bilinear elasto-plastic material model summarized in table 1 in comparison with stainless steel 316L used for fabrication of typical BE stents [38, 39]. This table also presents the geometrical properties of the RRR model and a nominal BE stent [22]. The von-Mises yield criterion and bilinear isotropic hardening rules are adopted here.

Simulating a tri-folded real angioplasty balloon calls for very high computational power, while also causing convergence problems. This is due to the need for a very refined mesh of the balloon and the introduction of self-contact in the balloon. To avoid these complexities, without sacrificing the deformation results, a simple elastic tube model is adopted. The presence of this tube is accounted for the time-varying exposure of surfaces of the RRR to pressure during expansion. The material properties of the balloon are assumed to be linear isotropic as follows: density 0.95 g cc^{-1}, modulus of elasticity 11 MPa and Poisson's ratio 0.42. Frictional forces between ring faces and the balloon are neglected for simplicity of the first-order calculations.

A ramped pressure of 150 KPa is applied to the inner walls of the balloon over 10 msec. These pressure levels are well below the typical inflation pressures of angioplasty balloons. The mean inner and outer diameters of the ring before expansion were 2.9 and 3.3 mm, respectively, and only a limited range of expansion is studied here. Both the balloon and the RRR are free to move radially (in the *X*–*Y* direction) while being constricted axially (fixed in the *Z* direction). This is to restrain the teeth going off-plane with respect to each other.

2.1.2. Results. Figure 3(*a*) presents the mean inner diameter of the RRR as a result of the balloon pressure during expansion. Figure 2(*b*) shows the von-Mises stress distribution plots around the teeth during tooth traversal. As indicated by figure 3(*a*), tooth traversal starts at around 90 KPa (point A) and finishes at 100 KPa (point B) followed by a smooth increase in the diameter of the RRR over time leading to a final mean inner and outer diameters of 3.6 and 3.84 mm, respectively. Furthermore, this figure presents the max von-Mises stress developed in the RRR over time during the expansion process. Figure 3(*b*) shows stress distribution plots over the deformed body of the RRR at the end of the expansion process. As demonstrated, the final status of the ring indicates the maximum stress levels lying well below the tensile strength of Nitinol (table 1).

In figure 3(*a*), the peak stress marked by point C, followed by a decrease in the stress levels, indicates occurrence of permanent plastic deformations in the RRR structure. To ensure safe interlock operation and ruling out excessive disfigurements of the teeth during expansion, plastic strains of these areas are studied more closely. For this reason, the

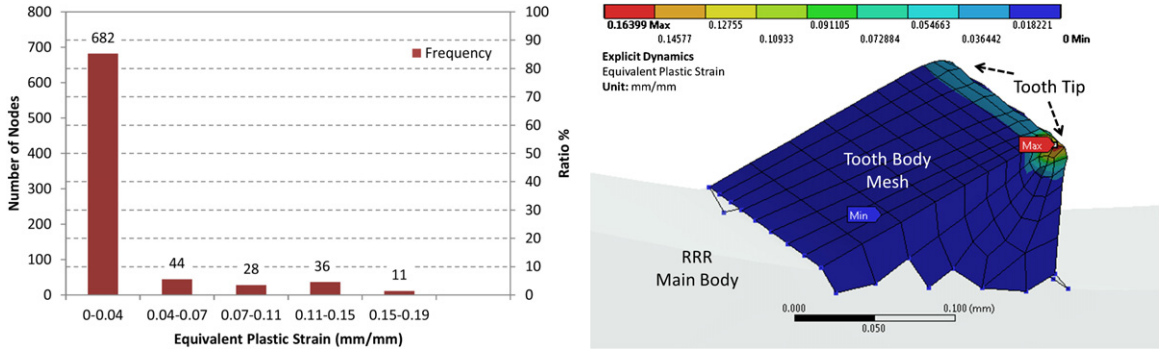

(*a*) (*b*)

Figure 4. Plastic strain results of the teeth, (*a*) Histogram of the distribution of plastic strain rate among 801 nodes of the elements of the teeth, (*b*) equivalent plastic strain plot of one of the teeth after completion of tooth traversal.

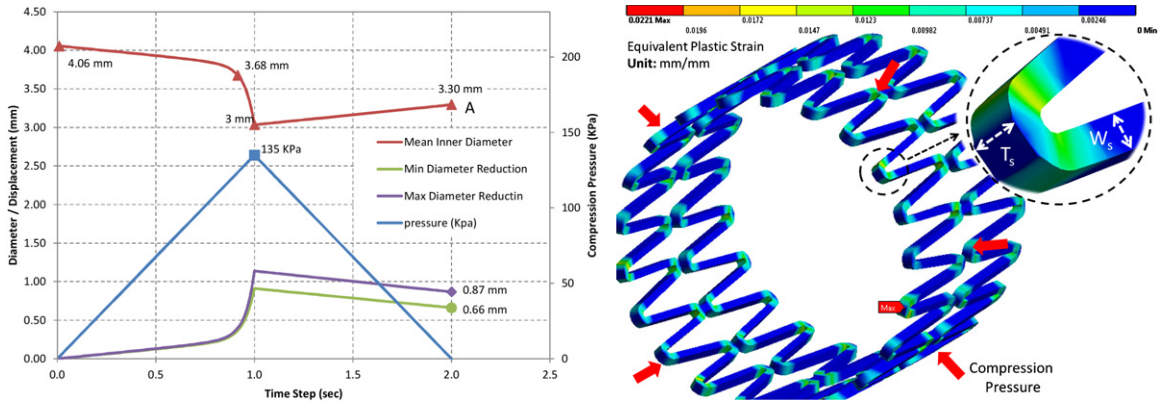

(*a*) (*b*)

Figure 5. Compression results of a two-column BE stent, (*a*) change of mean inner diameter, pressure and max and min diameter reduction over time, (*b*) plastic strain plots of the deformed model after removal of the compression pressure.

histogram of the distribution of equivalent plastic deformation of the elements of the teeth is presented in figure 4(*a*). As shown, about 85% of the elements in the teeth have less than 4% strain rate and this is despite more concentration of smaller elements at the tip of the teeth and the concentration of elements with higher strain rates at the tip area as shown in figure 4(*b*). Considering the very small average strain rate of 3% for the teeth elements, it is evident that the plastic deformations would have minimal effect on the overall structural integrity of the sawtooth structures. This statement is further confirmed by the deformed equivalent plastic strain plots of one of the teeth after completion of tooth traversal shown in figure 4(*b*).

Radial stiffness of luminal support is one of the most important measures of their performance after deployment [6]. In this section, a comparative analysis on the radial stiffness of the proposed RRR and a two-column typical BE stent (table 1), subject to a circumferential compressive pressure is conducted. The expanded geometries of both the BE stent (figure 5(*b*)) and the RRR (figure 6(*b*)) with mean inner diameters of 4 mm are first imported into a 3D static structural analysis. Next, a uniform compressive pressure of 135 KPa is applied to the outer surfaces of the geometries increased linearly over the first solution time step. In the second step, the pressure is linearly decreased to 0 KPa as shown in figure 5(*a*). Each one of the solution time steps is solved by a series of 100 sub-steps.

As the results in figure 5(*a*) show, the mean inner diameter of BE stent reduces linearly down to about 3.7 mm while the pressure is increasing. This trend is followed by a relatively much faster reduction in the diameter despite the linear increase of the pressure, which is an indication of plastic deformations. At pressure 135 KPa, about 44% of the CSA of the stent is lost due to the compression. By complete removal of the pressure, as noted by point A in figure 5(*a*), the stent still would not recover to its initial expanded state leading to about 34% loss of the initial CSA. Figure 5(*b*) shows the remaining plastic deformation plot of the stent after removal of the compression pressure at time step 2.

As presented in figure 6(*a*), subject to the same pressure profile, the RRR exhibits much less radial loss. At pressure 135 KPa, the RRR has lost only 0.07 mm of the initial diameter leading to about 3.4% reduction in CSA that is about 13 × less than that of the BE stent. The lost diameter is all recovered after removal of the pressure leading to no loss of cross-sectional area. This is also confirmed by the max von-Mises stress trend presented over time in figure 6(*a*). As indicated by figures 6(*a*) and (*b*), the stress levels over the loading and unloading periods are well below the yielding stress levels of the martensite Nitinol (table 1) ensuring the RRR withholding its structural and radial integrity under compressive loads such as the ones by lumens.

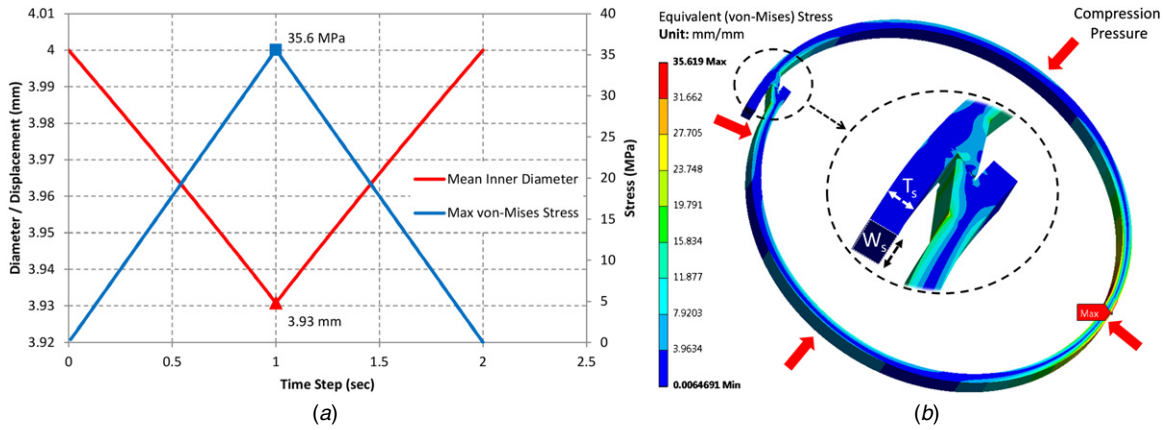

Figure 6. Compression results of RRR, (*a*) mean inner diameter, and max von-Mises stress over time, (*b*) plastic strain plots of the deformed model after removal of pressure.

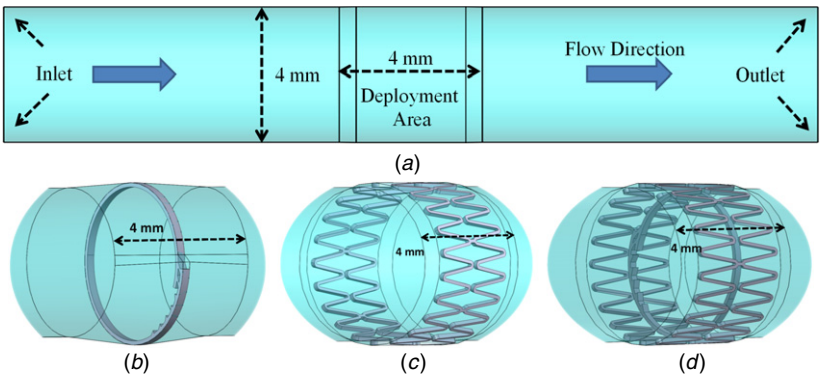

Figure 7. Fluid domain configurations for CFD analysis, (*a*) healthy lumen with the deployment area being marked, (*b*) stand-alone RRR deployment area, (*c*) BE stent deployment area, (*d*) integrated RRR & BE stent area.

The modeling results in this section are limited as the interactions between the simplified models of the RRR and the BE stent, and the surrounding lumen were not modeled. Nevertheless, these results are complimented by the experimental *in vitro* results in the next section by the inclusion of the effect of a silicon-based mock artery.

2.2. CFD analysis of the fluid flow

As mentioned before, stent design is shown to be one of the potentially critical factors affecting restenosis that is tissue regrowth after stent deployments [40]. A direct relationship between the alterations of hemodynamics, thereby changes in the wall shear stress distribution in the arteries post-deployment, and later restenosis has been established [41, 42]. In [35, 36] a strong relation between low wall shear stress (LWSS), less than 0.5 Pa, and neo-intimal hyperplasia and the resultant restenosis has been suggested. On the other hand, elevated shear stress (more than 1.5 Pa) is considered to be more beneficial and anti-proliferative of intimal cells [41–43]. This conclusion, led to a number of studies investigating the effect of different stent designs on the distribution of LWSS using CFD [44–49].

2.2.1. Material and methods. In this section, a comparison of the amount of areas subject to LWSS in the deployment area of three different supports is presented. The three supports deployed inside arteries with an inner diameter of 4 mm are as follows: (a) stand-alone RRR, (b) a nominal BE stent [22], (c) integrated RRR & BE stent. These configurations are shown in figure 7. The first two supports are expanded so that they provide an average inner diameter of 4 mm, which is identical to the natural diameter of the healthy artery. For the integrated RRR & BE stent as shown in figure 7(*d*), the BE stent mesh is expanded so it would provide an average inner diameter of 4 mm yet not considering the presence of the RRR. This is to study the effect of integration of RRR on the LWSS distributions without extra expansion of the lumen that would account for the presences of the RRR. Geometrical properties of the RRR and the BE stent are given in table 1.

The blood flow is considered to be steady, laminar and incompressible governed by the relations of conservation of momentum and mass [44]. These relations are solved by the commercial CFD package COMSOL (COMSOL Inc., Los Angeles CA, USA). The density of blood is considered to be $\rho = 1060$ kg m^{-3}. Non-Newtonian characteristics of the blood are considered by employment of Carreau model [44, 47]. Using this model, the shear-dependent dynamic viscosity of blood μ is expressed by

$$\mu = \mu_\infty + (\mu_0 - \mu_\infty)(1 + [\lambda\dot{\gamma}]^2)^{(n-1)/2}, \qquad (1)$$

where $\mu_0 = 0.25$ kg ms^{-1} and $\mu_\infty = 0.0035$ are the viscosities at zero and infinity shear rate, respectively, while

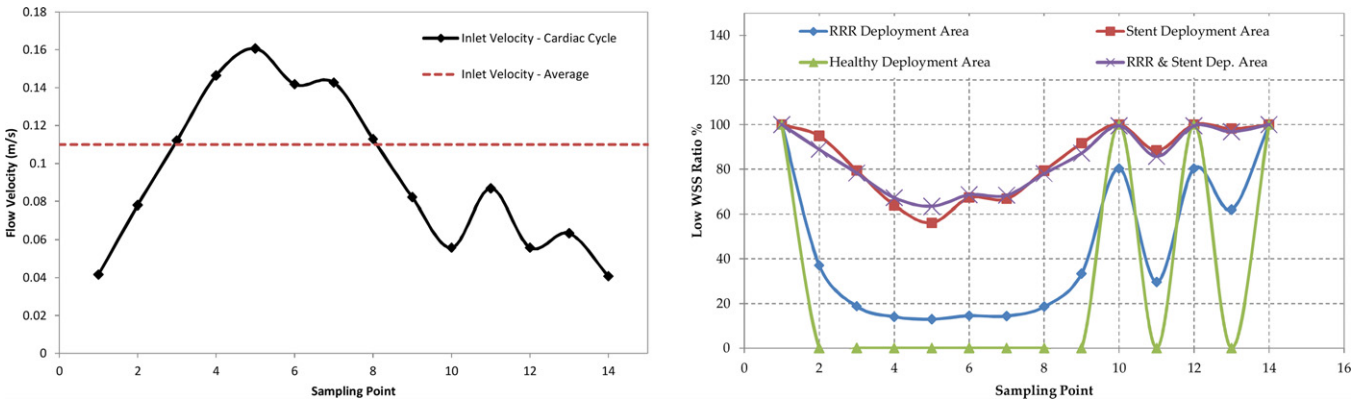

(*a*) (*b*)

Figure 8. Inlet velocity profile during one cardiac cycle and LWSS distribution during this cycle, (*a*) cardiac cycle, (*b*) ratio of the area subject to LWSS at the deployment area during one cardiac cycle for the support configurations of figure 7.

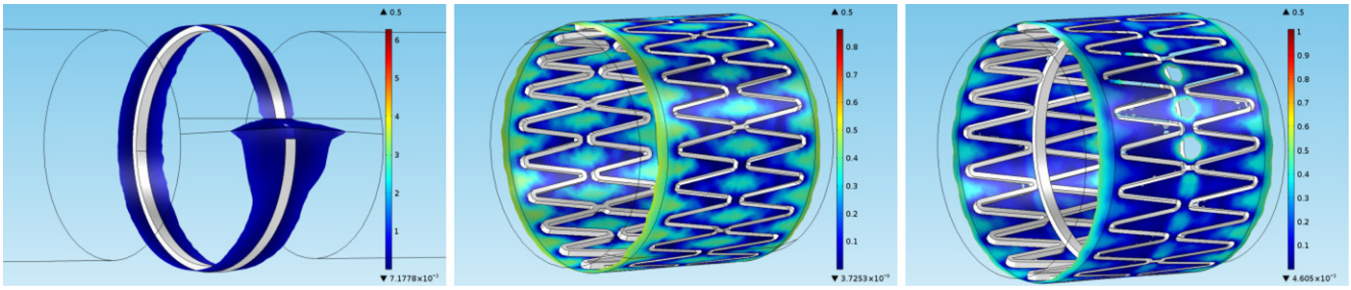

(*a*) (*b*) (*c*)

Figure 9. LWSS distribution at average inlet velocity at, (*a*) stand-alone RRR deployment area, (*b*) BE stent deployment area and (*c*) integrated RRR & BE stent deployment area.

$\lambda = 25.00$ s and $n = 0.25$ are material-dependent constants [44]. Simulations are performed for a full cardiac cycle [45] evaluated at 14 sampling points as shown in figure 8(*a*). Flow velocities are applied to the inlet while a zero-gauge pressure boundary condition is specified for the outlet. Fluid domain before and after the deployment areas were extended to result in a fully developed flow before entering the deployment domain. Moreover, a no-slip condition is defined on the walls, making all velocity components zero. The fluid domain is considered as rigid, which is a reasonable assumption for the stented arteries.

To ensure mesh independence, mesh at each 3D model was refined in multiple steps till changes in the results meet the mark of less than 3% change from one refinement level to the next. This resulted in the average element number of around 800 000 for each model including the free tetrahedral and quad boundary layer elements.

2.2.2. Results. Wall shear stress is determined by multiplying the shear rate and viscosity after completion of the solution. Figure 8(*b*) presents the ratio of luminal wall areas subject to LWSS (that is <0.5 Pa) to the total luminal wall area at the deployment area of the supports.

Figure 9 presents the LWSS distribution contour plots of the three support configurations of figures 7(*b*) to (*d*) in the deployment area, at the average flow velocity of 0.11 m s^{-1} denoted by an average line in figure 8(*a*).

As shown by figures 8(*b*) and 9, the stand-alone RRR support exhibits the least ratio of areas subject to LWSS at the deployment area compared to those of BE stent and integrated RRR & BE stent configurations. Moreover, the RRR & BE stent configuration shows a very similar LWSS distribution behavior to that of a single BE stent implicating minimal impact of the addition of RRR to a BE stent structure. In addition to the compression test results from the previous section, these results clearly show the merit of the RRR both as a stand-alone support and as an add-on to current BE stents.

3. Fabrication

As discussed earlier, the RRR devices are fabricated from Nitinol sheets with a thickness of 200 μm using a commercial μEDM system (EM203, Smaltec International, IL, USA). Although by the use of a rotational axis available in μEDM, it is possible to realize 3D designs such as the proposed final structure in figure 1(*a*), to reduce the likelihood of geometrical errors and follow the policy of minimal technology complexity, we feed a planar structure to the μEDM. The machined piece can later be transformed into the desired final structure with a number of repeatable steps. By decreasing the time of machining, less potential sources of error (X, Y and Z axis movements versus X, Y, Z and angular movements) and less material waste, this process makes mass bulk machining of RRRs realizable using sheet materials.

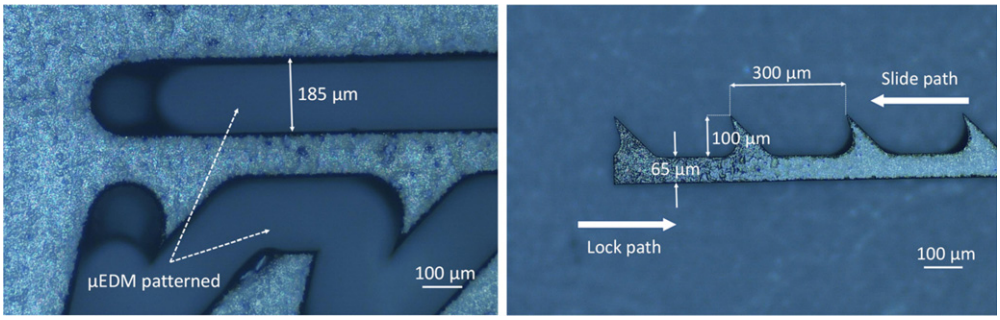

(*a*) (*b*)

Figure 10. μEDM patterned structure from the 200 μm thick Nitinol sheet, (*a*) one end of the through-hole structure before release of the strip, (*b*) other end of the strip detached from the sheet.

3.1. Machining

The μEDM patterning is conducted in oil with the conventional scanning method using cylindrical tungsten electrodes of approximately 150 μm thick in diameter. The scanning sequence is programmed to create the planar structure discussed earlier. Figure 10 shows the two ends of the 15 mm long planar structure of the device. Four up-right sliding teeth are arranged on one end of the strip, called the slide end, while at the other end, called the support end, there are seven facing down.

Due to the relatively large structure to be patterned, the process used the largest level of discharge energy available with the system. The time required to machine one RRR using machining conditions of voltage level = 100 V, capacitance = 3.3 nF, tool rotation speed = 3000 rpm and feed rate = 10 mm min^{-1} is approximately 12 h. This is quite slow due to the use of single tip electrode, but the planar fabrication allows potential use of batch-mode μEDM [50] in the future to enable volume production of the device so drastically decreasing fabrication time per RRR structure.

3.2. Shaping

To shape the planar strip to a ring structure, the setup in figure 11(*a*) is prepared and used. It is comprised of a stainless steel base on top of which a 4 mm thick, 4 cm long stainless steel rod is fixed. The strip is wound around the bottom of the rod where it meets the plane of the base (figure 11(*b*)). This is to ensure winding within the plane and to eliminate chances of torsional deformation within the structure during thermal training. The ring was fixed to the rod by an adhesive, yet to provide constant mechanical support in high treatment temperatures (around 500 °C), a stainless steel cap is used to encompass and fix the ring in its position.

The final structure after thermal treatment is demonstrated in figure 12(*a*) showing the ring in its fully dilated state with a mean inner diameter of 4 mm. The teeth A and B from the slid end will be removed from a final design resulting in a design resembling that of figure 1(*a*). This is to provide a smooth surface at the circumference of the RRR, where it contacts the inner walls of the lumen at the expanded state when the RRR is used as a stand-alone support. In this state, all the teeth from the support end will be facing inwards, and the teeth from the slide end are covered by the support end. For the prototype design at this stage, these teeth are included to compensate for the loss of any of the teeth due to possible fabrication defects.

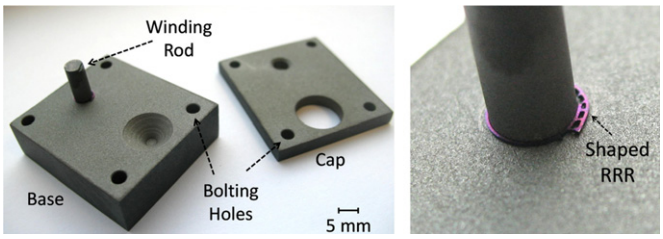

(*a*) (*b*)

Figure 11. RRR shaping and thermal treatment setup, (*a*) preview of the base and the cap, (*b*) the planar strip is wound around the 4-mm rod then fixed in place by a cap, enhanced image around the rod.

Integration of the RRR with a hosting stent is realizable via a single welding point to the stent mesh, figures 1(*b*) and 12(*b*). This is to provide enough support to stop migration of the RRR inside the stent while keeping the contact profile between the stent and the lumen intact.

Upon exertion of compressive forces on the circumference of the RRR, such as the condition within a vessel, at least two of the teeth, one from the slide end and the other from the support end, interlock and provide a strong scaffold to withstand the forces preventing recoil as described in the previous section. On the other hand, from a crimped state, upon balloon inflation the teeth can slide over each other facilitating the expansion of the ring.

3.3. Surface profile

The surface roughness of the shaped unpolished RRR in figure 12 is measured by an optical profiler (Wyko NT9100, Veeco) and compared with that of an unpolished BE stent laser cut from stainless steel 316L (Evasc Medical Systems Co., BC, Canada). Surface roughness of the RRR is measured for one cut face, where the machining is performed, and one base face that is the surface of the Nitinol sheet used for fabrication (figure 12). The measurements for the unpolished stent are performed on a base face. Table 2 presents the measurement parameters and the roughness measurements of these surfaces. As indicated by the average roughness measure (Ra), both the cut surface and the base surface exhibit similar

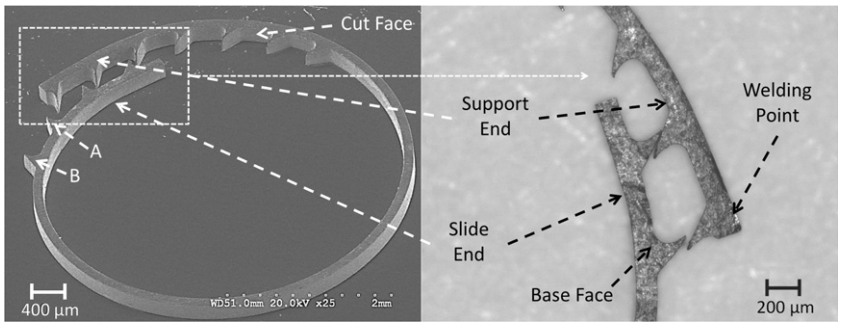

Figure 12. Shaped and thermally trained RRR, (*a*) full preview, teeth A and B are removed from a final design, (*b*) close-up image around the teeth. The teeth can slide over each other facilitating dilation, while they interlock in the recoil direction. The RRR can be integrated inside a hosting stent by a single welding point between the stent mesh and the support end. Cut and base surfaces are used for surface profiling.

Table 2. Surface roughness measurement parameters and values.

Measurement parameters			
Measurement length (μm)		158	
Measurement width (μm)		118	
Measurement mode		Vertical scanning interferometry (VSI)	
Surface measurements			
	RRR		BE stent
	Cut surface	Base surface	
Ra (nm)	580	560	433
Rq (nm)	734	713	555

roughness. Moreover, these values correspond with those of the unpolished BE stent.

Figure 13 shows the 3D surface profile of parts of the cut and the base surface areas of the RRR.

In order to decrease the sharp edges for better hydrophility and improving bio- and hemocompatiblity, further passivation steps such as electrochemical or mechanical polishing could be taken into account before clinical *in vivo* trials. These methods are currently used with current state-of-the-art alloy stents to reduce thrombogenicity while not compromising their structural integrity [17].

3.4. RRR patency

In order to evaluate the patency of the RRR in a dilated state, a comparison between the cross-sectional impact of the RRR and a typical commercial stent (TAXUS Liberte Coronary Stent, Boston Scientific, Boston, USA) is drawn in the following.

The average effective diameter of a scaffold (RRR or the commercial stent), D_{eff}, is expressed by

$$D_{\text{eff}} = D_{\text{exp}} - D_{\text{lost}} \,, \tag{2}$$

where D_{exp} is the mean outer diameter in the expanded state, and D_{lost} is the average diameter lost due to the strut thickness (T_s).

Given this relation, the patency gain as a measure of the efficiency of the device to accommodate fluid flow can be defined as follows:

$$G_P = \frac{A_C}{A_T} = \left(\frac{D_{\text{eff}}}{D_{\text{exp}}}\right)^2 \times 100\% \,, \tag{3}$$

where A_C is the average cross-sectional area patent to fluid flow, and A_T is the mean cross-sectional area of the implanted supporting structure. According to the measurements conducted in the next section, the average truss height of the commercial stent loop is 107 μm, which is in correspondence with the average strut thickness of 0.1 mm available in the literature [38] which results in a patency gain of $G_p = 90.603\%$. For the RRR, given it retains a fully or nearly fully dilated state after deployment, a higher limit on the average strut thickness can be calculated as

$$T_{s,avg} = T_{s,flat} + \frac{n\frac{t_h t_l}{2} + O_l(t_h(S_h + t_h))}{S_l} \,, \tag{4}$$

where $T_{s,flat} = 0.065$ mm is the thickness of the fabricated RRR strip where it does not have any teeth (figure 10), $n = 9$ is the total number of teeth in a final structure, $t_h = 0.1$ mm is the height of a tooth, $t_l = 0.1$ mm is the length of a tooth and O_l is the overlapping length of the two ends of the ring ($\sim$0.54 mm). Substitution into relations (4), then (2) and (3) results in the patency gain $G_p = 93.67\%$ that shows a 3.3% improvement over the commercial stent.

4. Experimental results

As mentioned in the previous section, two of the most important and competing trade-offs of an effective stent design are firstly high radial resistance against compressive forces, and secondly expandability within rated angioplasty pressures [6, 51]. In this section, the expandability of the fabricated RRR using an angioplasty balloon and recoil resistance characteristics of the device are experimentally evaluated. For these tests, the RRR is first manually crimped to have a mean outer diameter of 3 mm so that it can be easily inserted into a commercially available silicone-based mock artery (Dynatek Dalta Scientific Instruments, MO, USA). A mock artery with an inner diameter of 4 $\pm$ 0.2 mm and radial compliance of 6–8%, comparable to human arteries, is used for this experiment. Next, the ring is threaded by a deflated balloon (TAXUS Liberte MONORAIL, Boston Scientific, Boston, USA) with the nominal expanded balloon diameter of 4.5 mm. Having this ensemble residing inside the mock artery, the balloon is gradually inflated by increasing the pressure

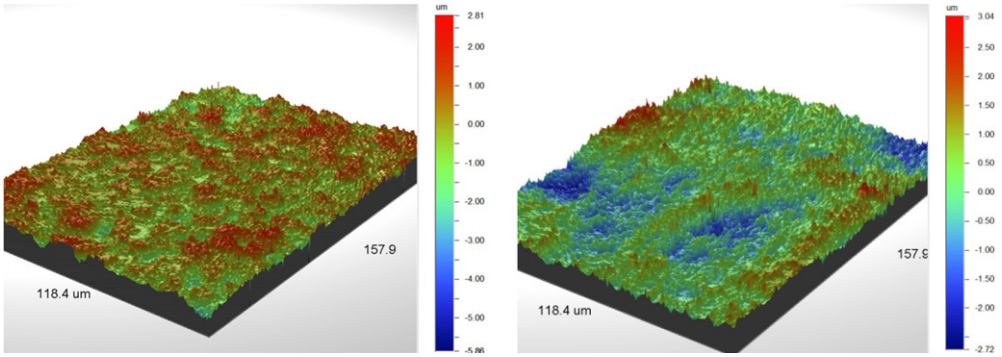

(*a*) (*b*)

Figure 13. Surface profile of RRR, (*a*) on the cut surface, (*b*) on the base surface.

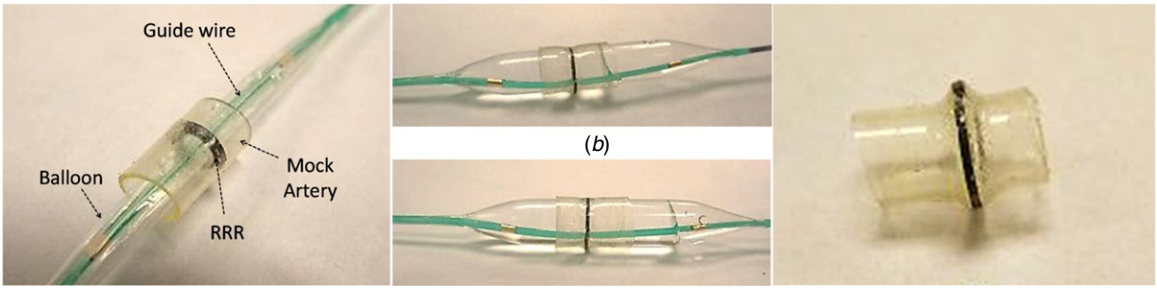

(*a*) (*b*) (*c*) (*d*)

Figure 14. *In vitro* balloon expansion of RRR, (*a*) the pre-inflation state, showing the RRR inside the mock artery threaded by the balloon, (*b*) balloon filled with deionized water inflated by raising the pressure to 3 Atm resulting in 4.7 mm mean outer diameter, (*c*) pressure raised to a maximum of 7 Atm resulting in 5 mm mean outer diameter, (*d*) balloon deflated and retracted from the mock artery resulting in 4.93 mm mean outer diameter.

inside while measuring the outer diameter of the RRR encompassed by the mock artery. The diameter measurements are implemented with a caliper (ABSOLUTE Digimatic, Mitutoyo, USA) taking the average of four measurements at each pressure stage up to 7 atm. Figure 14 shows the RRR at different conditions imaged during this test.

Average values of the RRR and the mock artery diameter obtained from measurements just before (5 mm) and after the deflation (4.93 mm) of the balloon indicate around 3% recoil in the CSA, significantly lower than those of commercial stents reported exhibiting 16% to 30% in CSA [7] or than the mean stent recoil of 13% in CSA reported in the literature [8].

As measures of performance, radial stiffness and bending compliance of stents are of paramount importance [51]. As per the RRRs, bending compliance is highly dependent on the hosting stent structure. Over the past decade, a number of methods to evaluate the radial strength of stents have been reported [52, 53]. To assess the radial stiffness of the RRR, a sample with the mean outer diameter of 4.6 mm is tested using the set-up shown in figure 15. The reaction forces of the sample caused by radial deformations are measured using a digital force gauge (DS2-2, Imada Inc., IL, USA) with 1 mN resolution held on a precision vertical linear stage. At the first step, the sample is compressed by the probe up to 500 μm with 10 μm displacement sub-steps while reading the reaction forces. In the next step, the relaxing forces are read while reversing the displacement of the probe. For comparison, a short sample of a 4.57-mm-dilated commercial BE stent made out of stainless steel 316L (TAXUS Liberte coronary stent, Boston Scientific, Boston, USA) with two columns cut out from the original stent body is also tested using the same set-up and loading procedure. As both samples in this set-up are not encompassed by any vessel, it is referred to as free-holding test.

The reason for comparison between a single RRR and two loops of a commercial stent is to have a similar width of material withstanding forces (two columns of around 100 μm thick commercial stent versus a single loop of 200 μm thick RRR). This is to have a fair comparison between the two by minimizing the effect of difference in strut width while considering the other sources of difference between the two structures including material properties and design, shown in table 3. Thickness and width values are given according to the average of four measurements under microscope.

The measurement results are presented in figure 16. As can be clearly observed in the results, the RRR demonstrates much higher radial stiffness overall, despite the fact that martensite Nitinol is much softer than stainless steel 316L. At 500 μm displacement, the reaction force from the RRR is $\sim$2.8 $\times$ greater than that of the commercial stent. Comparing highest slopes of the two trends during exertion of forces, it is also noticeable that the RRR exhibits early rigidity against compressional forces causing rapid increase of forces versus displacements compared with the commercial stent trend. Additionally, it is observable that the elastic recovery associated with the RRR is relatively in good accordance with that of the commercial stent.

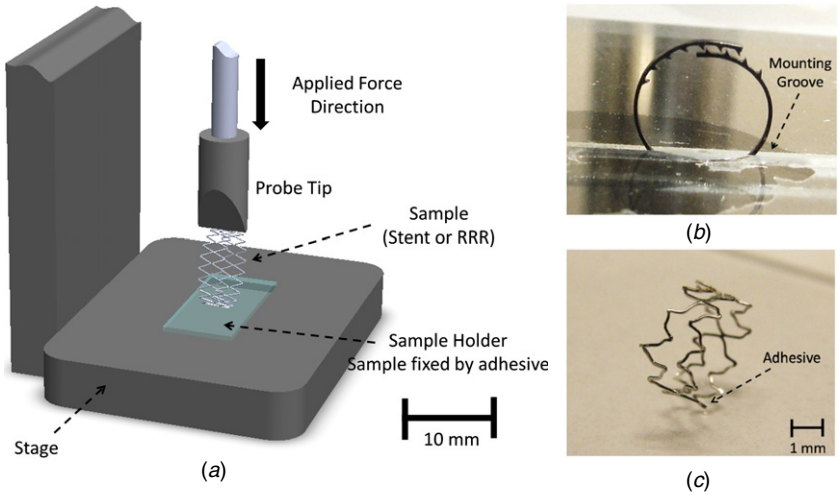

Figure 15. Set-up for radial loading test, (*a*) vertical positioning of samples under probe, (*b*) RRR mounted in a groove of the sample holder, (*c*) two-column sample of the commercial stent glued on the sample holder.

Table 3. Properties of the RRR and the two-column commercial stent samples used for compression test.

	RRR	**Commercial stent**
Number of columns	1	2
Outer diameter (mm)	4.6	4.57
Max. expansion pressure (atm)	7	8
Strut width (μm)	200	113
Strut thickness (μm)	65	107
Material	Martensite Nitinol	Stainless steel 316L, drug coated
Modulus of elasticity (GPa)	40	193
Loop design	Sliding ring with interlocking teeth	*Z*-shaped slotted tube with alternating bridges between the loops

One fact worth noting regarding the results with the RRR is that there is a small gap between the two outmost interlocking teeth at the initial state before loading starts (figure 15(*b*)). This gap causes the fast development of strain observed in the beginning of the radial displacement up to ~80 μm; upon the interlock of the two teeth, reaction forces start to grow rapidly as shown in figure 16. This gap arises due to the test condition that the RRR was held free.

To evaluate the device under compression, a likely condition in actual *in vivo* setting due to any recoil of a hosting stent and/or blood vessel, another stiffness test, referred to as the *in vitro* test, is conducted for the RRR being deployed inside a mock artery (figures 17(*a*) and (*b*)). Using a balloon inflated at 7 atm pressure, the RRR is expanded to a diameter of 4.9 mm, slightly larger than the diameter of the mock artery (~4.0 mm). Due to the recoil of the tube, the RRR rests in the state of the two teeth interlocked without any gap between them, unlike the case in the free-holding test.

This leads to the measurement results shown in figure 17(*c*) where reaction forces start to grow rapidly from the beginning of loading, demonstrating the RRR's full ability to resist external forces and minimize recoil at the expanded state. This can be observed by a comparison between the reaction force of point A in figures 16 and 17(*c*). Moreover, it can be seen from a comparison with figures 16 that higher forces are needed in the *in vitro* case to cause same displacements as in the free holding case. This is likely due to the presence of the additional layer of the artery around the device. Apart from that, upon unloading the RRR exhibits similar elastic recovery observed from the commercial stent[6] in the free-holding test. Considering the easier conformity, higher yielding point and comparable elastic recovery of the RRR (figures 16 and 17), it clearly outperforms the commercial stent in these aspects

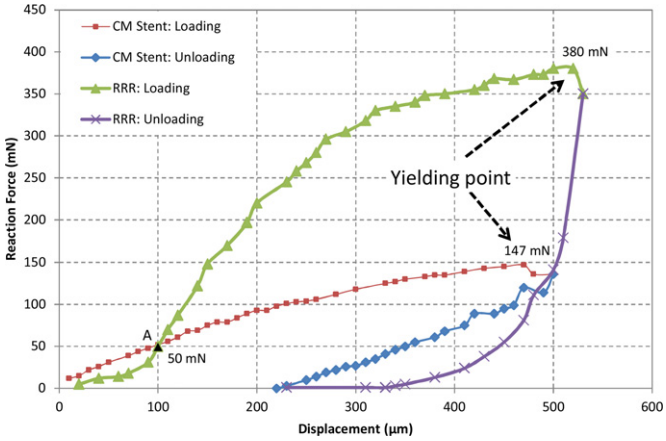

Figure 16. Free-holding loading test results, radial stiffness measurements of RRR versus a two-column commercial stent (CM Stent).

[6] TAXUS Liberte coronary stent, Boston Scientific, Boston, USA.

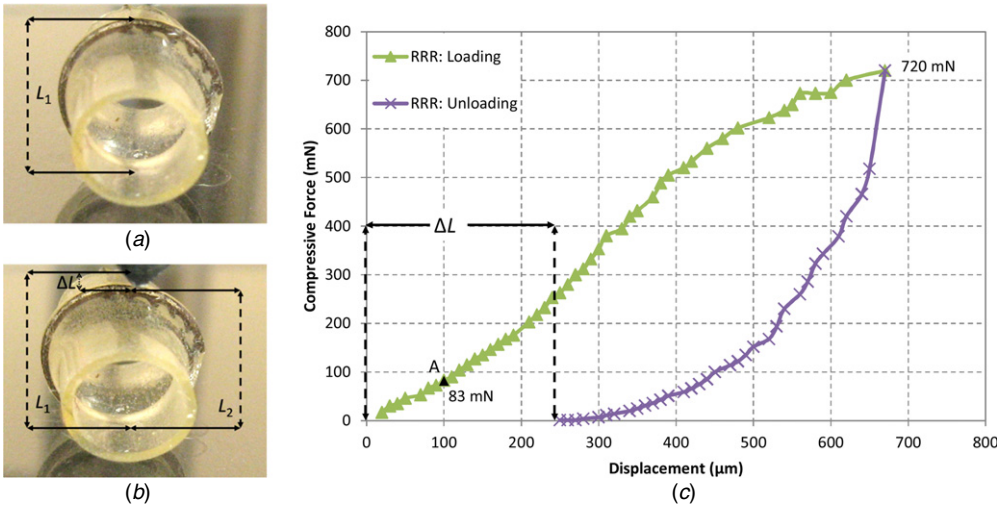

Figure 17. *In vitro* loading test results, radial stiffness measurement of the RRR deployed in an artificial artery, (*a*) the sample under the force probe before loading, (*b*) deformed sample after unloading, (*c*) measured reaction force versus displacement.

despite utilizing the softer martensitic Nitinol compared to the stainless steel in the commercial stent. The above results verify the effectiveness of the developed RRR device as a potential add-on to the existing stents to improve their recoil resilience while minimally affecting longitudinal flexibility and deployment procedures.

5. Conclusions and future directions

In this work, design modeling and fabrication of a viable recoil resilient lumen support for stenting applications has been investigated. The proposed structure called recoil resilient ring (RRR) is fabricated by μEDM technology cutting planar shapes from Nitinol sheets of 200 μm thickness. The simple planar design and subsequent shaping and training methods used facilitate batch processing and mass production of the structures. To be compatible with today's standard stenting tools and procedures, first-order simple models of the RRR are modeled to demonstrate expandability using an angioplasty balloon while maintaining structural integrity. Under circumferential compressive pressures, the FEA results indicate that the RRR exhibits only 3.4% loss of cross-sectional area, 13 $\times$ less than that of a typical balloon expandable stent. After removal of the pressure the balloon expandable stent lost 34% of the cross-sectional area due to plastic deformations while the RRR recovered completely.

The fabricated RRRs are then subjected to experimental *in vitro* expansion and stiffness tests. The free radial stiffness test measurements indicate 2.7 $\times$ higher radial rigidity of the RRR compared to that of a two-column stainless steel commercial stent. Considering the lower modulus of elasticity of Nitinol in martensitic form compared to stainless steel, and the comparable thickness and width of RRR and the commercial stent, the higher radial strength of RRR is delivered by the proposed interlocking mechanism.

The *in vitro* radial stiffness tests also show comparable elastic recovery of the RRR and the commercial stent. The proposed RRR is balloon expandable *in vitro* by 5–7 Atm pressure, well in the range of recommended *in vivo* pressures. The change in mean cross-sectional area after balloon deflation showed to be <3% for the RRR compared to the reported mean value of 13–30% associated with commercial stents.

Considering these specifications and the merit of RRRs, a series can potentially be welded by a single point inside a stent mesh, providing further scaffolding to specific areas and to the stent as a whole, while not sacrificing expandability or longitudinal flexibility. Considering these benefits compared to the added local thickness inside a stent due to the RRRs profile, the proposed structures bring a good trade-off between flexibility, deliverability and resilience.

Furthermore, use of shape memory alloy in the martensitic temperature range opens a path to other actuation and expansion methods such as application of heat or electric current as an extension of this work. Investigation of the long-term effects of the RRR on the surrounding tissue under pulsating contractions of the lumen (such as arteries), fatigue analysis of the structure as well as detailed study of the hemodynamic of the deployment area are the next important steps to be tackled by future studies.

Acknowledgments

This work was partially supported by the Natural Sciences and Engineering Research Council of Canada, the Canada Foundation for Innovation and the British Columbia Knowledge Development Fund. KT is supported by the Canada Research Chairs program. MSMA acknowledges financial support from Ministry of Higher Education Malaysia and Universiti Teknologi Malaysia, Malaysia. This research has also been funded by BUPA Postgraduate Travel Grant, and Research Abroad Scholarship, The University of Adelaide, Australia. The authors would like to thank Dr R Rashidi and Mr M Dahmardeh from University of British Columbia, Canada, for their assistance during development of this project. The authors would also like to thank Mr S Doe and Mr D Chugh from Ian Wark Research Institute, Australia, for access to the optical profilometer.

References

[1] Grech E D and Ramsdale D R 2002 *Practical Interventional Cardiology* (London: Martin Dunitz)

[2] Handler C and Cleman M 2006 *Classic Papers in Coronary Angioplasty* (London: Springer)

[3] Morgan R A and Walser E 2010 *Handbook of Angioplasty and Stenting Procedures* (London: Springer)

[4] Greene F L and Heniford B T 2010 *Minimally Invasive Cancer Management* (New York: Springer)

[5] Mehta A C and Dasgupta A 1999 Airway stents *Clin. Chest Med.* **20** 139–51

[6] Stoeckel D, Bonsignore C and Duda S 2002 A survey of stent designs *Minim. Invasive Ther. Allied Technol.* **11** 137–47

[7] Carrozza J P, Hosley S E, Cohen D J and Baim D S 1999 *In vivo* assessment of stent expansion and recoil in normal porcine coronary arteries: differential outcome by stent design *Circulation* **100** 756–60

[8] Danzi G B, Fiocca L, Capuano C, Predolini S and Quaini E 2001 Acute stent recoil: *in vivo* evaluation of different stent designs *Cathet. Cardiovasc. Interv.* **52** 147–53

[9] Duerig T and Duda S 2002 Stents: the future *Minim. Invasive Ther. Allied Technol.* **11** 135–6

[10] Hoffmann R and Mintz G S 2000 Coronary in-stent restenosis—predictors, treatment and prevention *Eur. Heart J.* **21** 1739–49

[11] Cantor W J, Peterson E D, Popma J J, Zidar J P, Sketch M H Jr, Tcheng J E and Ohman E M 2000 Provisional stenting strategies: systematic overview and implications for clinical decision-making *J. Am. Coll. Cardiol.* **36** 1142–51

[12] Alvarez W and Kapur N K 2005 Drug eluting stent technology *J. Pharm. Pract.* **18** 461–78

[13] Lowe H C, Oesterle S N and Khachigian L M 2002 Coronary in-stent restenosis: current status and future strategies *J. Am. Coll. Cardiol.* **39** 183–93

[14] Nickson C M, Doherty P J and Williams R L 2010 Novel polymeric coatings with the potential to control in-stent restenosis—an *in vitro* study *J. Biomater. Appl.* **24** 437–52

[15] Spanos V, Stankovic G, Tobis J and Colombo A 2003 The challenge of in-stent restenosis: insights from intravascular ultrasound *Eur. Heart J.* **24** 138–50

[16] Welt F G P and Rogers C 2002 Inflammation and restenosis in the stent era *Arterioscler. Thromb. Vasc. Biol.* **22** 1769–76

[17] Stoeckel D, Pelton A and Duerig T 2004 Self-expanding nitinol stents: material and design considerations *Eur. Radiol.* **14** 292–301

[18] Lagerqvist B, James S K, Stenestrand U, Lindbäck J, Nilsson T and Wallentin L 2007 Long-term outcomes with drug-eluting stents versus bare-metal stents in sweden *N. Engl. J. Med.* **356** 1009–19

[19] Lim D, Cho S-K, Park W-P, Kristensson A, Ko J-Y, Al-Hassani S and Kim H-S 2008 Suggestion of potential stent design parameters to reduce restenosis risk driven by foreshortening or dogboning due to non-uniform balloon-stent expansion *Ann. Biomed. Eng.* **36** 1118–29

[20] Rogers C and Edelman E R 1995 Endovascular stent design dictates experimental restenosis and thrombosis *Circulation* **91** 2995–3001

[21] Machado L G and Savi M A 2003 Medical applications of shape memory alloys *Braz. J. Med. Biol. Res.* **36** 683–91

[22] Bonsignore C 2011 *Open Stent Design* (Fermont, CA: Nitinol Devices and Components, Inc)

[23] Duerig T, Pelton A and Stöckel D 1999 An overview of nitinol medical applications *Mater. Sci. Eng.* A **273–275** 149–60

[24] Morgan N B 2004 Medical shape memory alloy applications—the market and its products *Mater. Sci. Eng.* A **378** 16–23

[25] Ali M S M and Takahata K 2011 Wireless microfluidic control with integrated shape-memory-alloy actuators operated by field frequency modulation *J. Micromech. Microeng.* **21** 075005

[26] Ali M and Takahata K 2010 Frequency-controlled wireless shape-memory-alloy microactuators integrated using an electroplating bonding process *Sensors Actuators* A **163** 363–72

[27] Kim B, Lee M G, Lee Y P, Kim Y and Lee G 2006 An earthworm-like micro robot using shape memory alloy actuator *Sensors Actuators* A **125** 429–37

[28] Mahendran S, Devarajan R, Nagarajan T and Madji A 2010 *A review of micro-EDM International Multiconference of Engineers and Computer Scientists* (Hong Kong: IAENG) pp 981–6

[29] Ho K H and Newman S T 2003 State of the art electrical discharge machining (EDM) *Int. J. Mach. Tools Manuf.* **43** 1287–300

[30] Mohd Abbas N, Solomon D G and Fuad Bahari M 2007 A review on current research trends in electrical discharge machining (EDM) *Int. J. Mach. Tools Manuf.* **47** 1214–28

[31] Takahata K 2009 *Micro Electronic and Mechanical Systems* (Vukovar: InTech) pp 143–64

[32] Murali M and Yeo S 2004 Rapid biocompatible micro device fabrication by micro electro-discharge machining *Biomed. Microdevices* **6** 41–5

[33] Kathuria Y P 2006 The potential of biocompatible metallic stents and preventing restenosis *Mater. Sci. Eng.* A **417** 40–8

[34] Takahata K and Gianchandani Y B 2004 A planar approach for manufacturing cardiac stents: design, fabrication, and mechanical evaluation *J. Microelectromech. Syst.* **13** 933–9

[35] Ku D N 1997 Blood flow in arteries *Annu. Rev. Fluid Mech.* **29** 399–434

[36] Ku D N, Giddens D P, Zarins C K and Glagov S 1985 Pulsatile flow and atherosclerosis in the human carotid bifurcation. Positive correlation between plaque location and low oscillating shear stress *Arterioscler. Thromb. Vasc. Biol.* **5** 293–302

[37] De Beule M, Mortier P, Carlier S G, Verhegghe B, Van Impe R and Verdonck P 2008 Realistic finite element-based stent design: the impact of balloon folding *J. Biomech.* **41** 383–9

[38] Li N, Zhang H and Ouyang H 2009 Shape optimization of coronary artery stent based on a parametric model *Finite Elem. Anal. Des.* **45** 468–75

[39] James F, Shackelford W A and Alexander W 2001 *CRC Materials Science and Engineering Handbook* 3rd edn (Boca Raton, FL: CRC Press)

[40] Kastrati A, Mehilli J, Dirschinger J, Pache J, Ulm K, Schühlen H, Seyfarth M, Schmitt C, Blasini R and Neumann F-J 2001 Restenosis after coronary placement of various stent types *Am. J. Cardiol.* **87** 34–9

[41] Traub O and Berk B C 1998 Laminar shear stress mechanisms by which endothelial cells transduce an atheroprotective force *Arterioscler. Thromb. Vasc. Biol.* **18** 677–85

[42] Malek A M, Alper S L and Izumo S 1999 Hemodynamic shear stress and its role in atherosclerosis *JAMA* **282** 2035–42

[43] DePaola N, Gimbrone M, Davies P F and Dewey C 1992 Vascular endothelium responds to fluid shear stress gradients *Arterioscler. Thromb. Vasc. Biol.* **12** 1254–7

[44] Hsiao H M, Lee K H, Liao Y C and Cheng Y C 2012 Cardiovascular stent design and wall shear stress distribution in coronary stented arteries *Micro Nano Lett. IET* **7** 430–3

[45] LaDisa J F, Olson L E, Guler I, Hettrick D A, Kersten J R, Warltier D C and Pagel P S 2005 Circumferential vascular deformation after stent implantation alters wall shear stress evaluated with time-dependent 3D computational fluid dynamics models *J. Appl. Physiol.* **98** 947–57

[46] Johnston B M, Johnston P R, Corney S and Kilpatrick D 2006 Non-Newtonian blood flow in human right coronary arteries: transient simulations *J. Biomech.* **39** 1116–28
[47] Zarandi M M, Mongrain R and Bertrand O F 2010 Non-Newtonian hemodynamics and shear stress distribution in three dimensional model of healthy and stented coronary artery bifurcation *Conf. COMSOL* (Boston: Comsol Inc) pp 1–5
[48] Frank A O, Walsh P W and Moore J E 2002 Computational fluid dynamics and stent design *Artif. Organs* **26** 614–21
[49] Balossino R, Gervaso F, Migliavacca F and Dubini G 2008 Effects of different stent designs on local hemodynamics in stented arteries *J. Biomech.* **41** 1053–61
[50] Takahata K and Gianchandani Y B 2002 Batch mode micro-electro-discharge machining *J. Microelectromech. Syst.* **11** 102–10
[51] Wholey M and Finol E 2007 Designing the ideal stent *Endovasc. Today* **6** 25–34
[52] Rieu R, Barragan P, Masson C, Fuseri J, Garitey V, Silvestri M and Roquebert P 1999 Radial force of coronary stents: a comparative analysis *Cathet. Cardiovasc. Interv.* **46** 380–91
[53] Flueckiger F, Sternthal H, Klein G E, Aschauer M, Szolar D and Kleinhappl G 1994 Strength, elasticity, and plasticity of expandable metal stents: *in vitro* studies with three types of stress *J. Vasc. Interv. Radiol.* **5** 745–50